On the interplay between downwelling, deep convection and mesoscale eddies in the Labrador Sea

Sotiria Georgiou[a,*], Carine G. van der Boog[a], Nils Brüggemann[b], Stefanie L. Ypma[a], Julie D. Pietrzak[a], Caroline A. Katsman[a]

[a]*Section of Environmental Fluid Mechanics, Faculty of Civil Engineering and Geosciences, Delft University of Technology, Delft, The Netherlands*
[b]*Faculty of Mathematics, Informatics and Natural Sciences, University of Hamburg, Hamburg, Germany*

Abstract

In this study, an idealized eddy-resolving model is employed to examine the interplay between the downwelling, ocean convection and mesoscale eddies in the Labrador Sea and the spreading of dense water masses. The model output demonstrates a good agreement with observations with regard to the eddy field and convection characteristics. It also displays a basin mean net downwelling of 3.0 Sv. Our analysis confirms that the downwelling occurs near the west Greenland coast and that the eddies spawned from the boundary current play a major role in controlling the dynamics of the downwelling. The magnitude of the downwelling is positively correlated to the magnitude of the applied surface heat loss. However, we argue that this connection is indirect: the heat fluxes affect the convection properties as well as the eddy field, while the latter governs the Eulerian downwelling. With a passive tracer analysis we show that dense water is transported from the interior towards the boundary, predominantly towards the Labrador coast in shallow layers and towards the Greenland coast in deeper layers. The latter transport is steered by the presence of the eddy field. The outcome that the characteristics of the downwelling in a marginal sea like the Labrador Sea depend crucially on the properties of the eddy field emphasizes that it is essential to resolve the eddies to properly represent the downwelling and overturning in the North Atlantic Ocean, and its response to changing environmental conditions.

Keywords: deep convection, downwelling, mesoscale eddy, surface forcing, Labrador Sea, Atlantic Meridional Overturning Circulation

1. Introduction

The Atlantic Meridional Overturning Circulation (AMOC) quantifies the zonally integrated meridional volume transport of water masses in the Atlantic Ocean. A prominent feature of the AMOC is an overturning cell where roughly 18 Sv (1 Sv = 10^6 m^3 s^{-1}, Cunningham et al. 2007; Kanzow et al. 2007; Johns et al. 2011) of water flows northward above 1000 m, accompanied by a southward return flow at depth. As the surface waters flow northward through the Atlantic Ocean, they become dense enough to sink before they return southward at depth.

This lower limb of the AMOC contains water masses that can be traced back to specific deep ocean convection sites (Marshall and Schott, 1999). There are few regions in the world oceans where deep convection occurs, and numerous studies have revealed that the most important ones are in the marginal seas of the North Atlantic (Dickson et al., 1996; Lazier et al., 2002; Pickart et al., 2002; Eldevik et al., 2009; Våge et al., 2011; de Jong et al., 2012; de Jong and de Steur, 2016b; de Jong et al., 2018).

Through the process of deep convection, dense waters are produced in the interior of the marginal seas, where the stratification is weak and the surface waters are exposed to strong heat losses (Marshall and Schott, 1999). While convection involves strong vertical transports of heat and salt, the interior of these marginal seas is known for a negligible amount of net downwelling. In particular, by applying the thermodynamic balance and vorticity balance to an idealized setting, Spall and Pickart (2001) pointed out that in a geostrophic regime, widespread downwelling in the interior of a marginal sea at high latitudes is unlikely, as it would have to be balanced by an unrealistically strong horizontal circulation. Instead, substantial downwelling of waters may occur along the perimeter of the marginal seas where the geostrophic dynamical constraints do not hold.

Using an idealized model, Spall (2004) demonstrated that significant downwelling indeed only occurs at the topographic slopes of a marginal sea subject to buoyancy loss. This downward motion yields an ageostrophic vorticity balance in which the vertical stretching term and lateral diffusion term near the boundary dominate (Spall, 2010). Straneo (2006b) considered the downwelling near the boundary from a different perspective, by developing an analytical two-layer model. In this study, a convective basin

*Corresponding author: Sotiria Georgiou , S.Georgiou@tudelft.nl, Environmental Fluid Mechanics, Stevingweg 1, 2628 CN, Delft, The Netherlands

is represented by two regions; the interior, where dense water formation occurs due to surface buoyancy loss, and a buoyant boundary current that flows around the perimeter of the marginal sea. It is assumed that instabilities provide the lateral advection of buoyancy from the cyclonic boundary current towards the interior required to balance the atmospheric buoyancy loss over the interior. This alongstream buoyancy loss of the boundary current reduces the density difference between the boundary current and the interior along the perimeter of the marginal sea. As a consequence, the thermal wind shear of the boundary current decreases in downstream direction, and continuity then demands the water to downwell at the coast (see also Katsman et al. (2018) and references therein).

Spall and Pickart (2001) argue that the magnitude of the buoyancy loss of the boundary current determines the amount of downwelling that occurs near the boundary. While the surface buoyancy loss contributes to this buoyancy loss, it is assumed to be mainly driven by eddies generated by instabilities of the boundary current (Spall, 2004; Straneo, 2006b).

Eddies shed from the boundary current also play an important role for the cycle of ocean convection and restratification. Deep convection occurs during wintertime in the southwest Labrador Sea (Clarke and Gascard, 1983; Lavender et al., 2000; Pickart et al., 2002; Våge et al., 2008). The dense water that is formed during the convection events, Labrador Sea Water (LSW), strongly contributes to the structure of the North Atlantic Deep Water, which in turn is a crucial component of the AMOC (Lazier et al., 2002; Yashayaev et al., 2007; Pickart and Spall, 2007; Lozier, 2012). Several studies show that the thermohaline characteristics of LSW are influenced not only by external parameters like the surface heat fluxes, but also by the baroclinic structure of the boundary current that enters the Labrador Sea (Spall, 2004; Straneo, 2006a), known as the West Greenland Current (WGC), and its interannual variability (Rykova et al., 2015).

In the Labrador Sea heat is carried from the WGC into the interior by Irminger Rings (IRs): large mesoscale eddies that are formed off the west coast of Greenland in a region characterized by a steep topographic slope (Lilly et al., 2003; Katsman et al., 2004; Bracco et al., 2008; Gelderloos et al., 2011). It has been recognised that the IRs strongly contribute to compensating the annual mean heat loss to the atmosphere that occurs in the Labrador Sea (Katsman et al., 2004; Hátún et al., 2007; Kawasaki and Hasumi, 2014).

From the above, it is clear that eddies are of immense significance for the downwelling as well as for the convection and the heat budget in the Labrador Sea. The dynamics of the downwelling and how it is related to the observed export of dense water masses is a topic of ongoing research, as the quantitative effects of the interplay between downwelling, eddies and convection are far from clear. For example, in a basin subject to buoyancy loss, one expects that an increase of the heat loss will result in denser and most likely deeper mixed layers. At first glance, this will increase the horizontal density gradients within the basin, strengthen the baroclinic instability of the boundary current and hence intensify the eddy field and the strength of the downwelling. This suggests a positive feedback of the increased eddy fluxes on the downwelling. However, the enhanced efficiency of eddies to restratify the interior after convection may provide a negative feedback on the convection and it is not clear a priori what the net effect will be.

Moreover, observations show that convected waters that originate from the Labrador Sea contribute to the lower limb of the AMOC (Rhein et al., 2002; Bower et al., 2009). This suggests that there has to be a connection between the convective regions (where these dense waters are formed) and the surrounding circulation near the boundary (where waters can sink) that has not been fully explored. Eddies provide a possible natural connection between these two regions.

The aim of this study is to assess the quantitative impacts of the eddy field on the downwelling in the Labrador Sea and its interaction with deep convection. We seek to gain more insight in the dynamics that control the downwelling in a convective marginal sea and its response to changing forcing conditions. Towards this goal, we use a highly idealized configuration of a high-resolution regional model in order to isolate specific processes and connect the outcomes with theory. In particular, we diagnose how the eddy field influences the downwelling by exchanging heat between a warm boundary current and a cold interior basin subject to convection. We compare our results to previous theories of downwelling dynamics. In addition, we use a passive tracer study to shed light into the pathways of the dense water masses and especially focus on the role of the eddies in determining these pathways. Finally, by using two sensitivity studies reflecting a milder and colder winter climate state, we test the sensitivity of the downwelling and the export of dense waters with regard to varying surface forcing.

The paper is organized as follows: the model setup and the simulations performed are described in section 2. The representation of deep convection and the characteristics of the downwelling are described in section 3. The response of the deep convection and the time mean downwelling to changes in the surface forcing is presented in section 4, followed by a discussion in section 5. The conclusions of this work are presented in section 6.

2. Model setup

2.1. Model domain and parameters

The numerical simulations performed in this study are carried out using the MIT general circulation model (Marshall et al., 1997) in an idealized configuration for the Labrador Sea. MITgcm solves the hydrostatic primitive equations of motion on a fixed Cartesian, staggered C-grid in the horizontal. The configuration of the model is an improved version of the one used in the idealized studies of Katsman et al. (2004) and Gelderloos et al. (2011), which now incorporates seasonal variations of both the surface forcing and the boundary current and enhanced vertical resolution.

The model domain is 1575 km in the meridional direction and 1215 km in the zonal direction. It has a horizontal resolution of 3.75 km in x and y direction (Fig. 1a), which is below the internal Rossby radius of deformation for the first baroclinic mode in the Labrador Sea (∼7.5 km, Gascard and Clarke 1983). The model has 40 levels in the vertical with a resolution of 20 m in the upper layers up to 200 m near the bottom. The maximum depth is 3000 m and a continental slope is present along the northern and western boundaries (Fig. 1a). Following Katsman et al. (2004) and Gelderloos et al. (2011), we apply a narrowing of the topography to mimic the observed steepening of the slope along the west coast of Greenland, which is crucial for the shedding of the IRs from the boundary current (Fig. 1a, Bracco et al. 2008). The continental shelves are not included. There are two open boundaries (each roughly 100 km wide), one in the east and one in the southwest, where the prescribed boundary current enters and exits the domain. All the other boundaries are closed (Fig. 1a).

Subgrid-scale mixing is parameterized using Laplacian viscosity and diffusivity in the vertical direction and biharmonic viscosity and diffusivity in the horizontal direction. The horizontal and vertical eddy viscosity are $\mathrm{A_h} = 0.25 \times 10^9\ \mathrm{m^4\ s^{-1}}$ and $\mathrm{A_v} = 1.0 \times 10^{-5}\ \mathrm{m^2\ s^{-1}}$ respectively, while the horizontal diffusion coefficient is $\mathrm{K_h} = 0.125 \times 10^9\ \mathrm{m^4\ s^{-1}}$. The vertical diffusion coefficient is described by a horizontally constant profile which decays exponentially with depth as $\mathrm{K_v(z) = K_b + K_0 \times e^{(-z/z_b)}}$, where

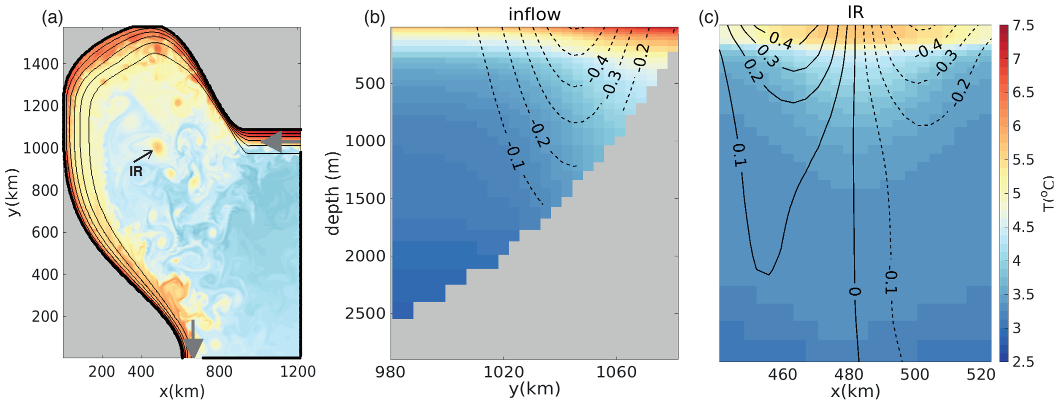

Fig. 1: (a) Snapshot of the sea surface temperature (SST) for the reference simulation (referred to in the text as REF). Black contours outline the bathymetry, the contour interval is 500 m starting from the isobath of 500 m. The grey arrows represent the inflow/outflow, where the boundaries are open ($x_{\mathrm{inflow}} = 1215$ km, $y_{\mathrm{inflow}} = 978.75 - 1083.75$ km and $x_{\mathrm{outflow}} = 611.25 - 708.75$ km, $y_{\mathrm{outflow}} = 3.75$ km) (b) Section across the inflow region (at x = 1215 km) showing the annual mean temperature (T_{in}, in °C) and meridional velocity (U_{in}, in m s^{-1}, black contours). (c) Zonal section of an example Irminger Ring in the REF simulation by means of temperature (shading, in °C) and meridional velocity (black contours, in m s^{-1}). This Irminger Ring is visible in the SST snapshot in the basin interior (x=443-525 km and y=1012.5 km) in (a).

$K_b = 10^{-5}$ m^2 s^{-1}, $K_0 = 10^{-3}$ m^2 s^{-1} and $z_b = 100$ m. Temperature is advected with a quasi-second order Adams-Bashforth scheme. In case of statically unstable conditions, convection is parameterized through enhanced vertical diffusivity ($K_v = 10$ m^2 s^{-1}). A linear bottom drag with coefficient 2×10^{-4} m s^{-1} is applied.

Following Katsman et al. (2004), the model is initialized with a spatially uniform stratification, $\rho_{\mathrm{ref}}(z)$, representative of the stratification in the western Labrador Sea in late summer along the WOCE AR7W section. Only temperature variations are considered in the model, so this stratification is represented by a vertical gradient in temperature, $T_{\mathrm{ref}}(z)$, calculated from $\rho_{\mathrm{ref}}(z)$ using a linear equation of state: $\rho_{\mathrm{ref}}(z) = \rho_0[1 - \alpha\ (T - T_{\mathrm{ref}}(z))]$, where $\rho_0 = 1028$ kg m^{-3} and α the thermal expansion coefficient ($\alpha = 1.7 \times 10^{-4}$ °C^{-1}).

The effects of salinity are not incorporated in the model. In reality, salinity does affect the properties of deep convection in the Labrador Sea, as the IRs shed from the boundary current carry cold, fresh shelf waters at their core (e.g., Lilly and Rhines, 2002; de Jong et al., 2016a). As shown in for example Straneo (2006a) and Gelderloos et al. (2012), the contribution of this lateral fresh water flux to the buoyancy of the Labrador Sea interior impacts the convection depth, and large salinity anomalies may in fact be partly responsible for observed episodes when deep convection shut down (Belkin et al., 1998; Dickson et al., 1988). However, since we focus here on the underlying dynamics that control the downwelling and its response to changing forcing conditions, the effects of salinity are omitted in the model for simplicity.

2.2. Model forcing

At the eastern open boundary, an inflow representing the WGC is specified by a meridional temperature field $\mathrm{T_{in}(y, z)}$ and a westward flow $\mathrm{U_{in}(y, z)}$ in geostrophic balance with this prescribed temperature (Katsman et al., 2004). Although the WGC consists of cold, fresh Arctic-origin waters and warm, salty waters from the Irminger Current (Fratantoni and Pickart, 2007) we only incoporate in the model density variations associated with the latter part. The cool, fresh surface waters are omitted, since they are found on the continental shelf, which is not included in our idealized bathymetry (Fig. 1a). The time-mean structure of this warm boundary current is shown in Fig. 1b. The boundary current follows the topography and flows cyclonically around the basin. The seasonal variability of the WGC seen in observations (Kulan and Myers, 2009; Rykova et al., 2015) is represented in the model by adding a sinusoidal seasonally varying term to the inflow conditions based on these observations ($\Delta \mathrm{U_{max}} = 0.4$ cm s^{-1} that peaks in September and attains its minimum in March). At the southern open boundary an Orlanski radiation condition (Orlanski, 1976) for momentum and tracers is applied.

At the surface, only a temporally and spatially varying surface heat flux is applied, which is an idealized version of the climatology of WHOI OAFlux project (Yu et al., 2008). The strongest heat loss occurs on the northwestern side of the basin (Fig. 2), and its amplitude decays linearly away from this heat loss maximum (white marker in Fig. 2b). The net annual heat loss over the entire model domain of the reference simulation (hereinafter REF) is -18 W m^{-2}. The time dependence of the amplitude of the surface heat fluxes (Fig. 2c) is also based on the observations, ranging from -320 W m^{-2} (January) to 140 W m^{-2} (July) at the location of the heat loss maximum.

One of the main objectives of this study is to investigate how changes in the surface heat fluxes influence the evolution of convection, eddy activity and the magnitude of the downwelling. For this reason, we perform

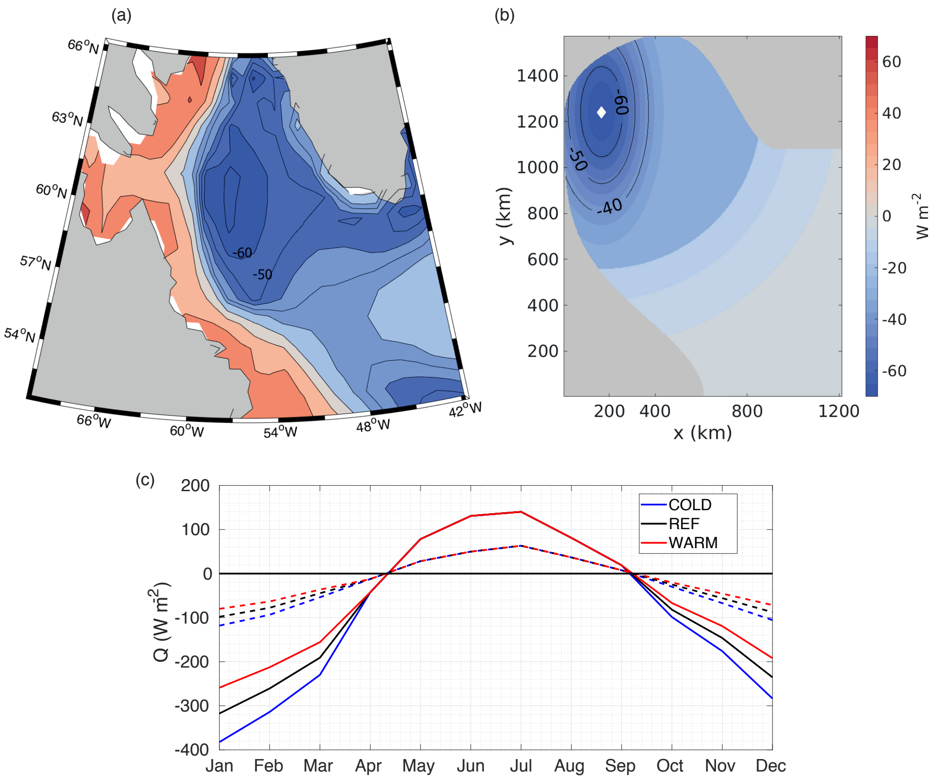

Fig. 2: (a) 1983-2009 mean of heat flux from the climatology of WHOI OAFlux project (Yu et al., 2008). (b) Annual mean surface heat flux applied to the model. Q<0 means cooling of the sea surface, Q in W m^{-2}. (c) Seasonal cycle of the amplitude of the heat flux at the location where the amplitude is maximum (white marker in b, solid lines) and the mean over the basin (dashed lines) for the three different simulations (black: REF, red: WARM and blue: COLD).

sensitivity studies, in which we change the atmospheric cooling in wintertime by 50% with respect to the reference simulation (Fig. 2c). The net annual heat loss over the entire model domain for these simulations with a colder and warmer wintertime regime (hereinafter COLD and WARM) is -25 and -12 W m^{-2} respectively or a 33% increase (28% decrease) in heat loss with respect to REF. In agreement with Gelderloos et al. (2012) and Moore et al. (2012), the mean winter heat loss (December-February, at the location of the heat loss maximum) is between -170 to -250 W m^{-2} in these simulations.

2.3. Model simulations

All the simulations are performed for a period of 20 years in which each model year is defined as 12 months with 30 days each for simplicity. The 2-day snapshots and the monthly means of all diagnostics are stored. For our analysis, we use the snapshots from the last five years of the simulations phase (i.e. model years 16 to 20).

Earlier studies have identified three types of eddies that may play a role for the dynamics of the Labrador Sea (Chanut et al., 2008; Gelderloos et al., 2011; Thomsen et al., 2014): the large Irminger Rings (IR) shed near the west coast of Greenland, convective eddies (CE) and boundary current eddies (BCE) that arise on fronts surrounding the convection region in winter and on the front between the boundary current and the interior, respectively. The latter two typically have a scale on the order of the Rossby deformation radius, and are much smaller than the IRs. At a resolution of 3.75 km we barely resolve these mesoscale CE and BCE. However, the IR are well represented in our model simulations.

A snapshot of the sea surface temperature for REF (Fig. 1a) illustrates that in the idealized model, warm core IRs are formed at the west coast of Greenland, where the slope is steep. A cross section of a representative IR is shown in Fig. 1c. The maximum velocity in the IR ranges between 0.5 and 0.8 m s^{-1} and the radius is approximately 30 km. This is in line with the observational studies of Lilly et al. (2003) and de Jong et al. (2014) who find maximum velocities between 0.3 to 0.8 m s^{-1} and diameters of 30-60 km. The temperature anomaly at the core of the modelled IR (representative of its buoyancy anomaly; recall that salinity effects are omitted) reaches at 1500 m. Moreover, the average temperature between 200 and 1000 m is 4.25 °C, which is in good agreement with the observed vertical structure of IRs as characterized by de Jong et al. (2014).

Fig. 3a shows the timeseries of the basin-mean temperature for the simulations. The impact of the seasonal cycle of the applied surface heat flux is evident. For all the simulations, after $\sim$ 10-15 years of integration the basin-mean temperature reaches a quasi-equilibrium. In this model, such an equilibrium can only be reached if the lateral advection of heat efficiently balances the heat that is lost to the atmosphere. A heat budget analysis indicates that this idealized model can reproduce the balance between the lateral heat advection and the surface heat flux (Fig. 3b and 3c), as proposed by Straneo (2006b) and Spall (2012). Although the mean heat advection and the eddy heat advection mostly cancel each other (Fig. 3d and Fig. 3e), the eddy heat advection dominates in the interior while the heat advection by the mean flow dominates within the boundary current. The eddy heat advection clearly shows the expected transport from the boundary to the interior (Fig. 3d). The negative contribution of the mean heat advection in the northern part of the domain may seem puzzling at first. However, similar negative contributions are seen in the model studies by Saenko et al. (2014) and de Jong et al. (2016a). We assume that this is a consequence of the fact that most eddies are anticyclones, and that they tend to follow a preferred path from east to west. As a result, the mean heat advection term contains a mean contribution of this "train of buoyant eddies". Once the eddies have detached from the boundary current, they move westward and cool along their path, which corresponds to a negative contribution to the mean heat advection. As a consequence, the eddies are responsible for an interior warming and the mean flow is responsible for a warming along the boundary. Both are necessary to balance the heat loss that occurs over the interior as well as over the boundary current. In addition, a cross section of the eddy heat advection over the interior confirms that the eddies transport a significant amount of heat into the interior at depths down to 500m (Fig. 3f).

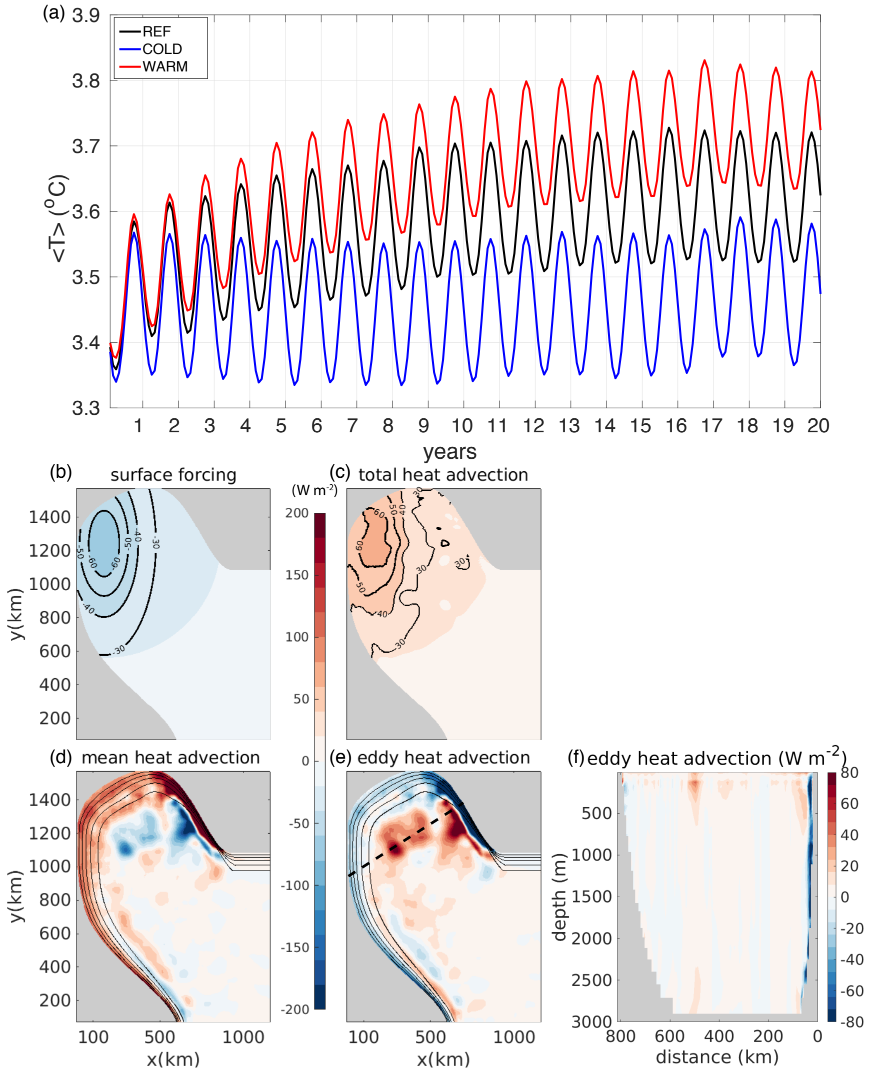

Fig. 3: (a) Timeseries of the basin-mean temperature of all simulations. (b-e) Depth-integrated terms of heat budget (in W m^{-2}) for the REF simulation (average over years 16-20): (b) surface heat flux (Q), (c) total heat advection (sum of mean and eddy component), (d) mean heat advection, $\nabla \cdot (\overline{\mathbf{U}}\overline{\mathrm{T}})$, and (e) eddy heat advection, $\nabla \cdot (\overline{\mathbf{U}'\mathrm{T}'})$. Overbars denote the five year means, primes the anomalies with this respect to this mean and $\mathbf{U} = (\mathrm{u}, \mathrm{v}, \mathrm{w})$ is the velocity vector. In (d) and (e) the black contours outline the bathymetry, the contour interval is 500 m starting from the 500 m isobath. (f) Eddy heat advection (in W m^{-2}) over the section indicated by the black dashed line in (e).

From the above and earlier studies with a similar version of the model (Gelderloos et al., 2011) it is evident that with this set of parameters the model is able to resolve the main characteristics of the eddy field, and to capture the properties of the mesoscale eddies (in particular the IRs). Although with the horizontal resolution of 3.75 km the sub-mesoscale eddies are not fully resolved in our model, we consider it appropriate for this study since we focus on the dynamics of the downwelling in the presence of mesoscale eddies.

3. Deep convection and downwelling in the basin

First, we examine the location and the size of the deep convection area and its connection to the properties of the eddy field for the reference simulation. We also investigate the characteristics of the downwelling, which is expected to peak in regions of high eddy activity, as discussed in section 1.

3.1. Properties of the mixed layer depth and eddy field

We calculate the mixed layer depth (MLD), following Katsman et al. (2004), as the depth at which the temperature is 0.025 °C lower than the surface temperature (equivalent to a change in density of 5×10^{-3} kg m^{-3}). The black contours in Fig. 4a show the winter (February-March, FM) mean patterns of the mixed layer depth (MLD) averaged over the last 5 years of the reference simulation (REF). The deepest convection is found in the southwestern part of the Labrador Sea, reaching depths of 1700 m. Note that the deepest mixed layers are not located where the maximum heat loss is applied (blue contours in Fig. 4a). A mean hydrographic section across the domain in late spring (May, Fig. 4b) shows that in this idealized model the convected water is found between the isopycnals of $\sigma = \rho - 1000 = 28.32 - 28.40$ kg m^{-3}. In addition, the surface layer is getting warmer at this time suggesting the beginning of the restratification phase as seen in observations (Lilly et al., 1999; Pickart and Spall, 2007). Overall, in REF the location and the depth of the convection area agree well with observations (Lavender et al., 2000; Pickart et al., 2002; Våge et al., 2009; Yashayaev and Loder, 2009) and complex high-resolution model simulations (Böning et al., 2016), certainly considering the idealizations applied in the model.

In REF, IRs propagate from their formation site near the coast towards the interior, as is shown in Fig. 5a by means of the relative vorticity at the surface. Their signal is weaker but still evident in deeper layers (Fig. 5b-d). This is in agreement with the example cross-section of an IR (Fig. 1c), which displays a vertical extent of 1000-1500 m. The IRs carry buoyant water from the boundary current into the interior Labrador Sea and

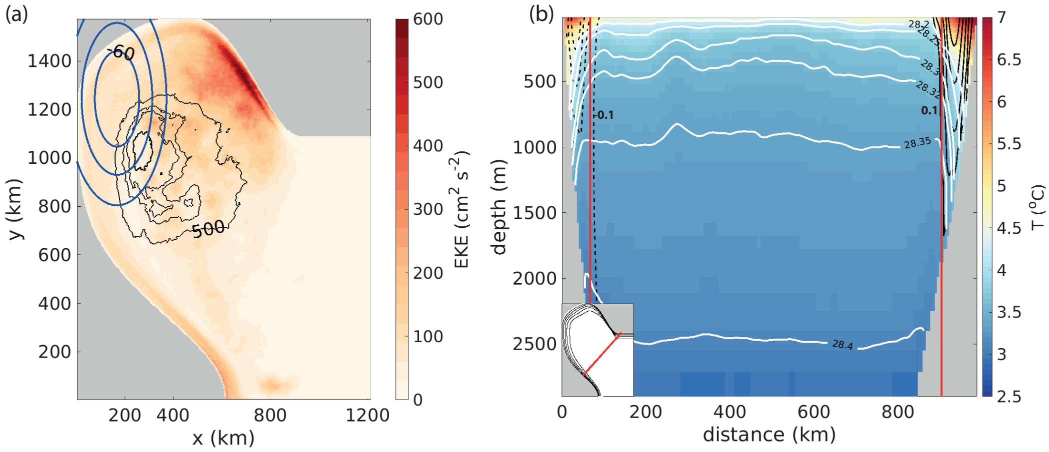

Fig. 4: (a) Mean eddy kinetic energy (EKE in cm^2 s^{-2}, shading) superimposed on the contours of the winter mixed layer depth (MLD in m, contour interval is 500 m) for REF. Blue contours denote the annual mean surface heat fluxes in W m^{-2} that have been applied to the simulation (contour interval is 10 W m^{-2}). (b) Late spring (May) mean temperature (shading, in °C) and density $\sigma = \rho - 1000$ (in kg m^{-3}; contour interval is 0.05 kg m^{-3}) over a section indicated by the red line in the inset figure, for REF. The section is plotted against distance from the west coast (km). Positive (negative) velocity contours are shown in black solid (dashed) lines (contour interval is 0.1 cm s^{-1}). The vertical red line indicates the limits of the boundary current based on the barotropic streamfunction. Values are averaged over years 16-20.

they effectively limit the extent of convection. To illustrate the extent of the impact of the IRs, we use the surface eddy kinetic energy, defined as $\mathrm{EKE} = \frac{1}{2}\,\overline{(\mathrm{u}'^{\,2} + \mathrm{v}'^{\,2})}$, where the overbar indicates the time averaged values of the five years considered and the primes are the deviations from the 5-year mean fields (shading in Fig. 4a). The EKE has a maximum of 625 cm^2 s^{-2} near the West Greenland continental slope and fades away offshore in a tongue-like shape. Its magnitude and pattern are in quantitative agreement with studies that derive EKE from altimetry (Prater, 2002; Lilly et al., 2003; Brandt et al., 2004; Zhang and Yan, 2018). Enhanced EKE is also observed along the Labrador coast with maximum values of 200 cm^2 s^{-2}, which is also associated with local instability of the boundary current (Brandt et al., 2004).

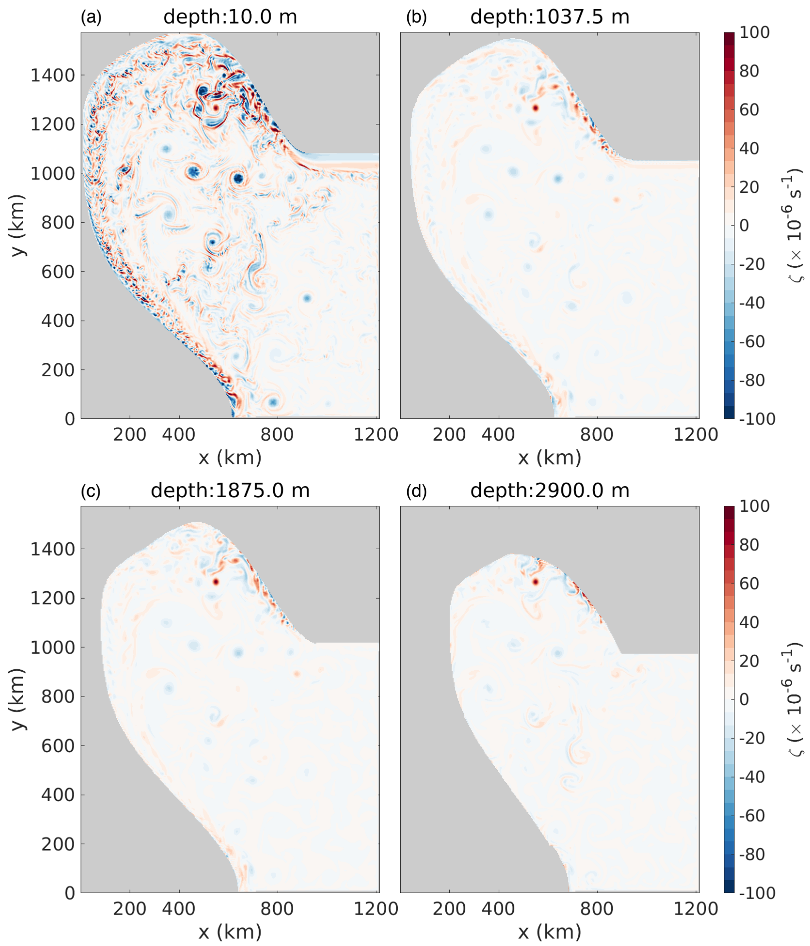

Fig. 5: Snapshot of the relative vorticity ($\zeta = \frac{\partial v}{\partial x} - \frac{\partial u}{\partial y}$, in 10^{-6} s^{-1}) for REF at the beginning of year 18 of the simulation at a depth of (a) 10.0 m, (b) 1037.5 m, (c) 1875.0 m and (d) 2900.0 m.

It is noteworthy that this highly idealized configuration is able to produce a realistic surface EKE and mixed layer, with regard to depth, location and extent (Fig. 4a). These mixed layer properties are not prescribed, in contrast to the study by Gelderloos et al. (2011), in which a convective patch was artificially created in the domain in a similar configuration of the model. Together with Fig. 3, this indicates that the current model setup captures the physical processes that are essential to the cycle of convection and restratification in the Labrador Sea, and hence is suited for this type of process study.

3.2. Vertical velocities and downwelling

To analyze the downwelling in the basin, we first calculate the time-mean vertical velocity integrated over the total domain and within four areas (Fig. 6a). Each of these areas is characterized by different dynamics: area 1 is the region where the IRs are formed, area 2 is the region where the strongest heat loss is applied, area 3 is the region in the southwest part of the domain where the second EKE maximum is found (Fig. 4a) and area 4 defines the interior, where the bottom is flat. In particular, the distinction between the interior and the boundary current areas is based on a cutoff value for depth (i.e. 2900m). The western edge of area 1 is defined to be well downstream of the EKE maximum.

It appears that in this idealized model an overturning is present. The net vertical transport over the total domain is downward (black line in Fig. 6b). It amounts to 3.0 Sv and peaks at a depth of 1000 m.

The horizontal distribution of the time-mean vertical velocities at this depth of maximum downward transport (i.e. 1000 m) in REF (Fig. 6c) shows two regions of strong vertical velocities along the lateral boundaries: one close to the steepening of the slope at the northeastern part of the domain and one close to the Labrador coast. This finding that high values of vertical velocity occur in a narrow area close to the lateral boundaries, in particular in areas characterized by elevated surface EKE (Fig. 4a), is in line with results from several idealized model studies (Spall and Pickart, 2001; Spall, 2004, 2010; Pedlosky and Spall, 2005) and global model studies (Luo et al., 2014; Brüggemann et al., 2017; Katsman et al., 2018). The outcome that the west coast of Greenland (area 1) and the Labrador coast (area 3) are identified as regions of enhanced downwelling again highlights the importance of the eddies for the dynamics of the Labrador Sea (see Fig. 4a).

Fig. 6b, which shows the vertical transport as a function of depth integrated over the full domain and the four areas, confirms that indeed the net downward transport seen in the model takes place in areas 1 and 3. The downwelling peaks in area 1 at a depth of 1000 m (green line in Fig. 6b) and amounts to 3.4 Sv, while in area 3 it amounts to 1.0 Sv at a depth of 1525 m. The areas 2 and 4 are characterized by a small net upwelling despite the fact that these two areas are subjected to the strongest surface heat loss. Focusing on the formation area of the IRs, we next analyze the vertical velocity over a cross section in area 1 (Fig. 6d). It is evident from this figure that the mean vertical transports in the interior are very low (at a distance greater than 60 km from the coast). Similarly to Spall (2004), the downwelling is concentrated close to the boundary, while there is an upwelling region farther offshore. This cell-like structure is what is expected from boundary layer dynamics (Pedlosky and Spall, 2005). Overall, as shown in Fig. 6b, the net transport in this area is downward.

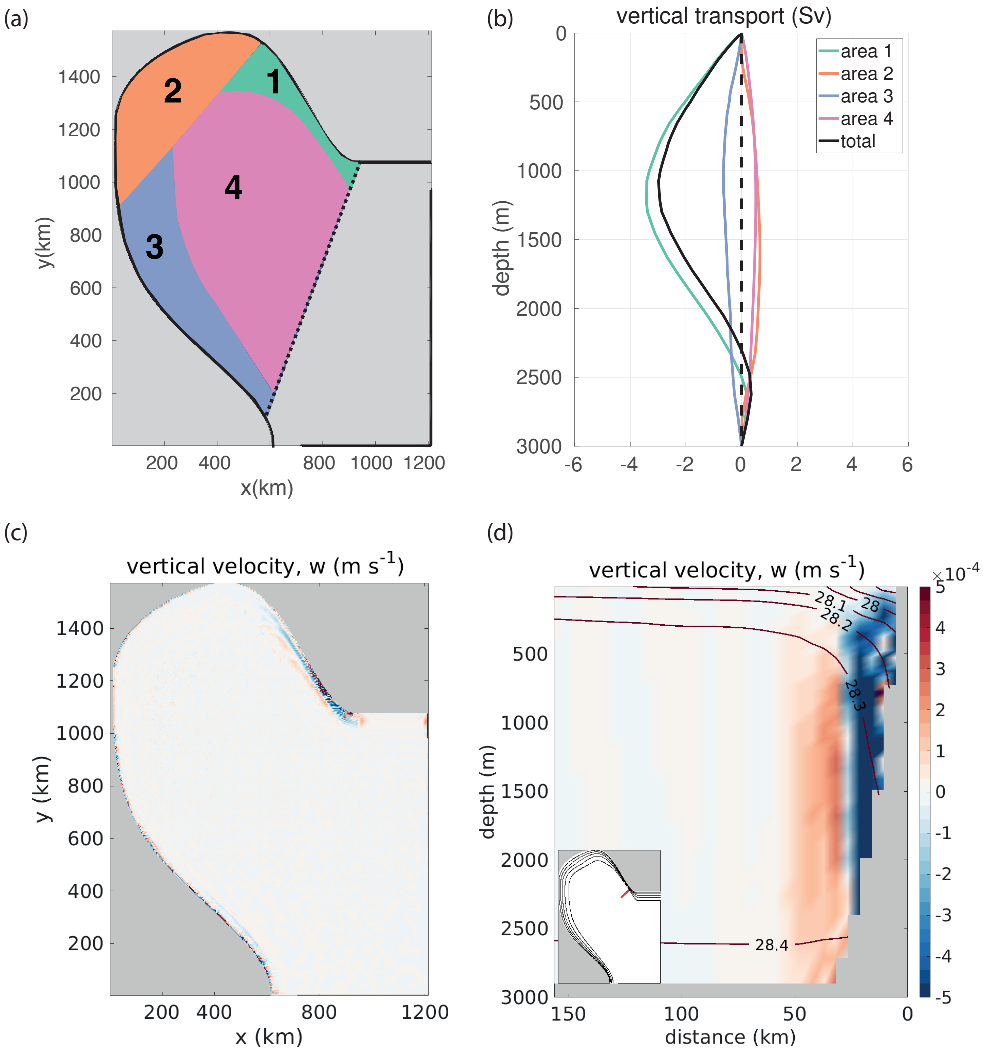

Fig. 6: (a) Definition of four areas (see text for detailed description). The total area of our interest is defined by the dashed line. (b) Vertical transport in depth space over the total domain and for the four areas (color-coded according to the map in (a)) for the REF simulation. (c-d) Vertical velocity at (c) 1000 m depth and (d) over a section across the boundary current near Greenland, indicated by the red line in the inset figure. The section is plotted against distance from the coast (km). Values are averaged over years 16-20.

3.3. Spreading of dense waters

A counterintuitive aspect that stands out from this analysis is the fact that the strongest downward motions occur at the lateral boundaries: a region associated with relatively buoyant waters rather than dense waters, while at the same time it is clear from observations that dense, convected waters contribute to the overturning circulation (Rhein et al., 2002; Bower et al., 2009).

To investigate the spreading of the dense waters, we released a passive tracer at the core of the convection area. The tracer is initialized with a value of 1 in a cylinder of a radius 190 km and from the surface to a depth of 1575 m (inset in Fig. 7a) at the beginning of year 16. The maximum depth for the initialization of the tracer corresponds well to the depth of the winter (February-March) mixed layer of the modelled year 16. It is monitored for a period of five years. After one year, the tracer is found in deeper layers in the section across the domain (Fig. 7a). During winter, the tracer is brought to deeper layers by convection, but by the end of the year its concentration is still bounded by the isopycnals of the convected water (i.e. $\sigma = 28.32 - 28.40$ kg m^{-3}, Fig. 4b). The tracer is directly advected into the boundary current at the western side of the basin (Fig. 7b-f), similarly to the export route suggested by Brandt et al. (2007). However, this export route mainly occurs at shallower depths ($z < 1575$m), while in deeper layers the tracer also moves towards areas 1 and 2 (Fig. 7d-h, more details on the evolution of the concentration of the passive tracer can be found in the movie in the supplementary material). This tracer advection is clearly steered by the eddy field. Once the tracer reaches area 1, which has been characterized as downwelling region, it can be advected by the mean boundary current (supplementary material) and exported out of the Labrador Sea following the boundary current (Straneo et al., 2003).

This view is supported by the time evolution of the vertical distribution of the tracer averaged over the four areas that is shown in Fig. 8. The tracer reaches area 1 after 4 months and only at depths larger than 500 m (Fig. 8a). It peaks after 13 months at a depth of 1675 m and then reduces gradually over time. Although the tracer is partly initialized in area 2 (Fig. 8b), its concentration peaks after 14 months and at a depth of 1412.5 m. This provides an indication that the tracer that reaches area 1 at depth is then advected by the mean boundary current towards area 2, and thereby contributes in the increase of the tracer concentration in area 2. Notably, the tracer peaks at shallower depths in area 2 than in area 1. This suggests that it follows the isopycnals, which are rising along the boundary in all areas (Fig. 4b and Fig. 7a). In area 3, the amount of tracer decreases from the start and hardly penetrates deeper than the initialization depth (Fig. 8c). This is in line with the view that the tracer in area 3 is predominantly directly exported by the boundary current (Fig. 7c-d). Lastly, in area 4 the amount of tracer reduces slowly over time (Fig. 8d).

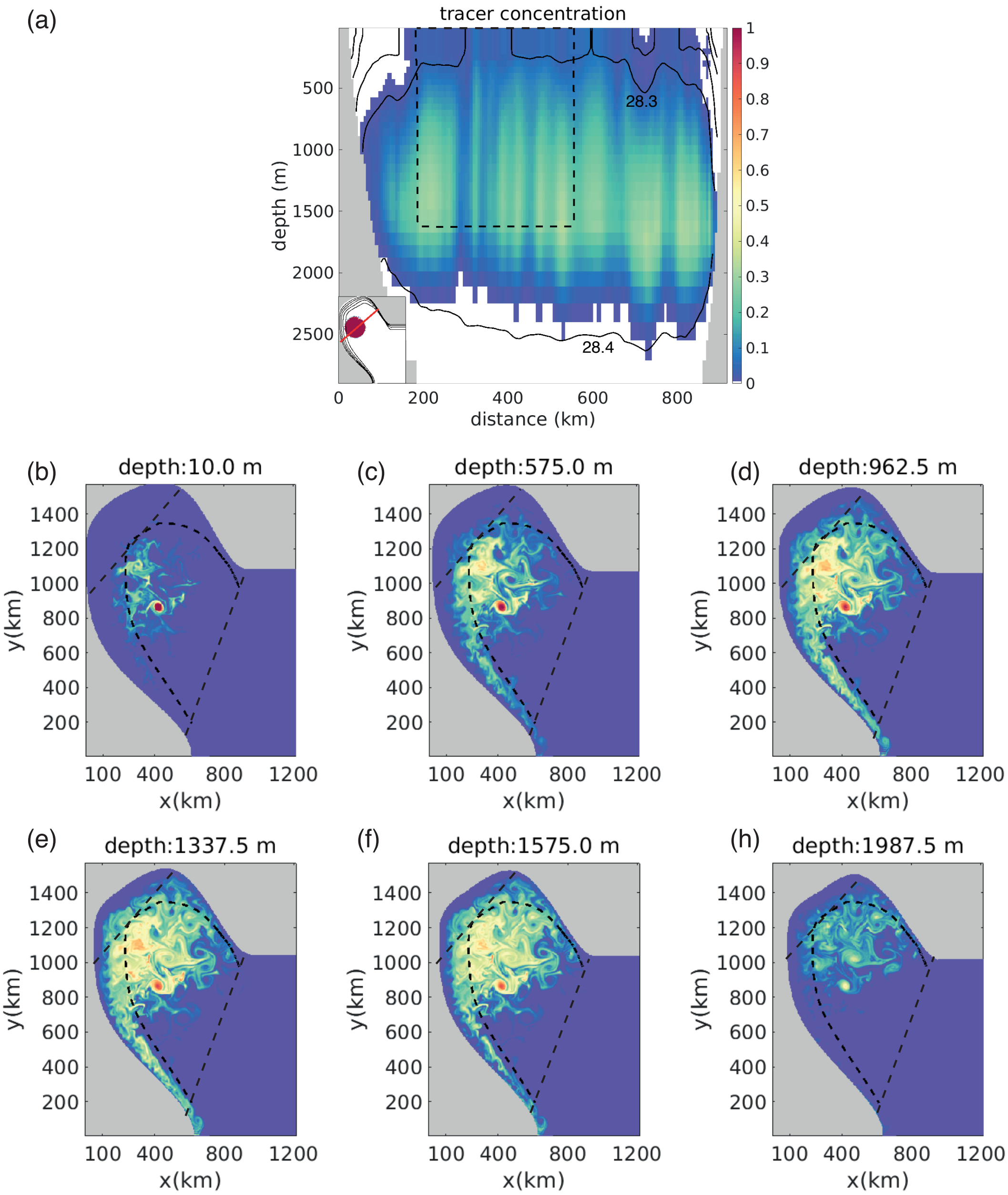

Fig. 7: (a) Cross section of the vertical distribution of the passive tracer at the end of year 16 for REF, at the section indicated by the red line in the inset figure, together with the isopycnal surfaces (in kg m^{-3}, black contours). The passive tracer is released at the beginning of year 16 over a cylinder that coincides with the convection area (dashed lines and inset figure). (b-h) Snapshots of the concentration of the passive tracer 5 months after its release at a depth of (b) 10.0 m, (c) 575.0 m, (d) 962.5 m, (e) 1337.5 m, (f) 1575.0 m and (h) 1987.5 m. Black dashed lines denote the areas defined in Fig. 6a.

Fig. 5 shows that the signal of the eddies extends to large depths, in line with the observational study by Lilly and Rhines (2002). A feature that stands out in Fig. 7b-h is a small area (centered at x = 425 km and y = 865 km) with a peak tracer concentration that extends down to 2000m, which is tracer trapped in the core of an IR. This feature should not be mistaken for an indication that westward travelling IRs capture the dense waters. This specific IR was present in the region where the tracer was initialized, and hence the tracer was added to its core. The tracer subsequently remains captured in the eddy (see movie in the supplementary material). Nevertheless, the eddies do seem to indirectly govern the tracer advection. The tracer transport towards the boundary occurs because of the strong shear that is present in the velocity field around the eddies, and is strongest close to the region where the eddies are shed.

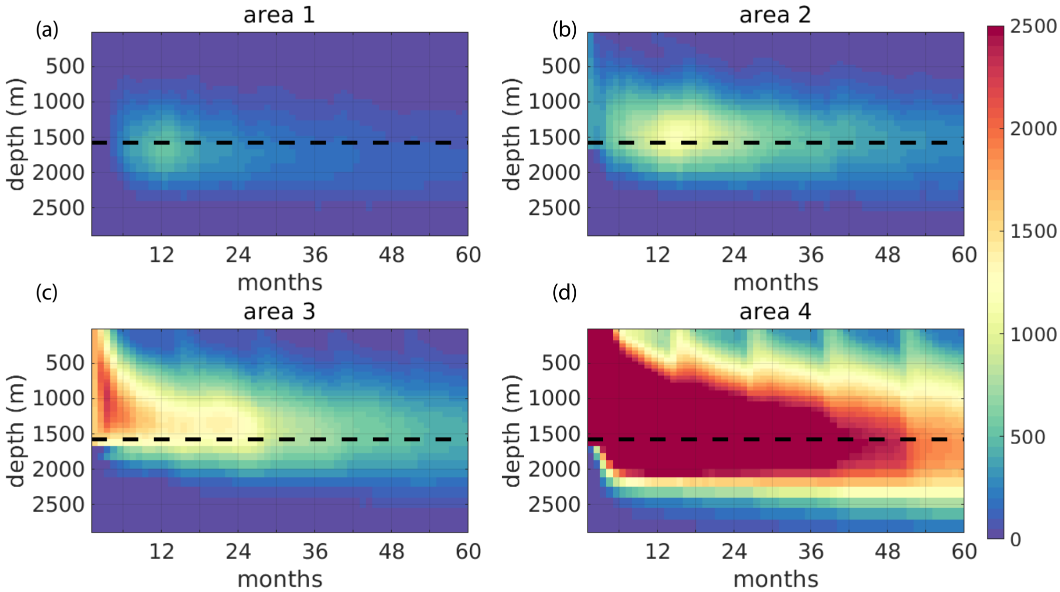

Fig. 8: Time evolution of the total amount of passive tracer in depth, integrated over (a) area 1, (b) area 2, (c) area 3 and (d) area 4 for REF. The black dashed line denotes the initial maximum depth of the tracer. The areas are defined in Fig. 6a.

4. Sensitivity to winter time surface heat loss

In this section, we assess the response of the eddies, convection and downwelling in two sensitivity simulations, in which the surface forcing is modified (see section 2.2 for details). Although the lateral eddy heat flux still balances the surface heat loss when the surface heat flux is changed in simulations COLD and WARM, as indicated by the regular seasonal cycle in the basin mean temperature (Fig. 3), it is expected that the properties of both the MLD and the EKE change. First, we focus on the response of the convection and the eddy field in both simulations. Next, we assess the impact of the changes in the surface forcing on the downwelling and the spreading of dense waters.

4.1. Response of convection and the eddy field

Under the scenario of a stronger winter surface heat flux (COLD), one expects that the winter mixed layer deepens, that the convection region becomes wider, and that denser waters are produced. In addition, one also expects that as the temperature gradient between the interior and the boundary current increases due to stronger surface cooling, the eddy activity is enhanced (Saenko et al., 2014; de Jong et al., 2016a). Fig. 9a and Fig. 9c illustrate that when the surface heat loss is increased, EKE is indeed more intense near the Greenland coast with a maximum of 750 $cm^2\ s^{-2}$, and the MLD becomes deeper, reaching depths of 2100 m. In WARM, the EKE is weaker (maximum value 575 $cm^2\ s^{-2}$, Fig. 9b and Fig. 9d) and the reduced surface heat loss results in a much shallower mixed layer, reaching depths of 960 m, and a narrower convective area. The model displays an asymmetric response of the MLD to changes in the heat flux: the same percentage change in the applied surface forcing results in changes of +25% (Fig. 9c) and -45% (Fig. 9d) in the maximum depth of the winter mixed layer. This asymmetry can be partly attributed to the stratification, which increases at larger depths, and partly to the changes in the baroclinicity of the boundary current and the associated eddy activity as is discussed in the next paragraph.

Fig. 10 shows the eddy advection of heat for the three simulations. The eddy component of the advective heat flux is negative for the boundary current, while it is positive for the interior, once more confirming that the eddies extract heat from the boundary current and transport it towards the convection region. Also, the mean advection of heat in COLD and WARM changes (not shown). As for REF (Fig. 3b-e), it almost cancels the eddy advection. The total heat advection balances the applied surface heat loss, confirming that an equilibrium is reached. Strong eddy heat fluxes originate from the regions with enhanced values of EKE that have been discussed in section 3 (i.e. along the Labrador coast and in particular at the steep West Greenland continental slope). In COLD, not only the eddy activity is stronger than in the REF case (Fig. 9c) but also the eddy advection of heat from the boundary current into the interior is enhanced (Fig. 10a). Thus, as the surface cooling is stronger, the restratification of the water column after convection also intensifies, counteracting the deepening of the convection induced by the increased surface heat loss. However, this negative feedback is apparently weaker than the direct impact of the increased surface heat loss on the convection depth, as the MLD deepens. In WARM, the surface heat loss is smaller, but the eddy heat advection into the interior weakens as well (Fig. 10c). The eddy heat advection averaged over the interior (area 4, Fig. 6a) amounts to 24 W m^{-2}, 28 W m^{-2} and 46 W m^{-2} for WARM, REF and COLD respectively. This confirms that changes in the eddy heat advection into the interior are not simply propotional to the changes in the applied heat loss and that the surface heat fluxes and lateral eddy fluxes combined regulate the properties of the convection.

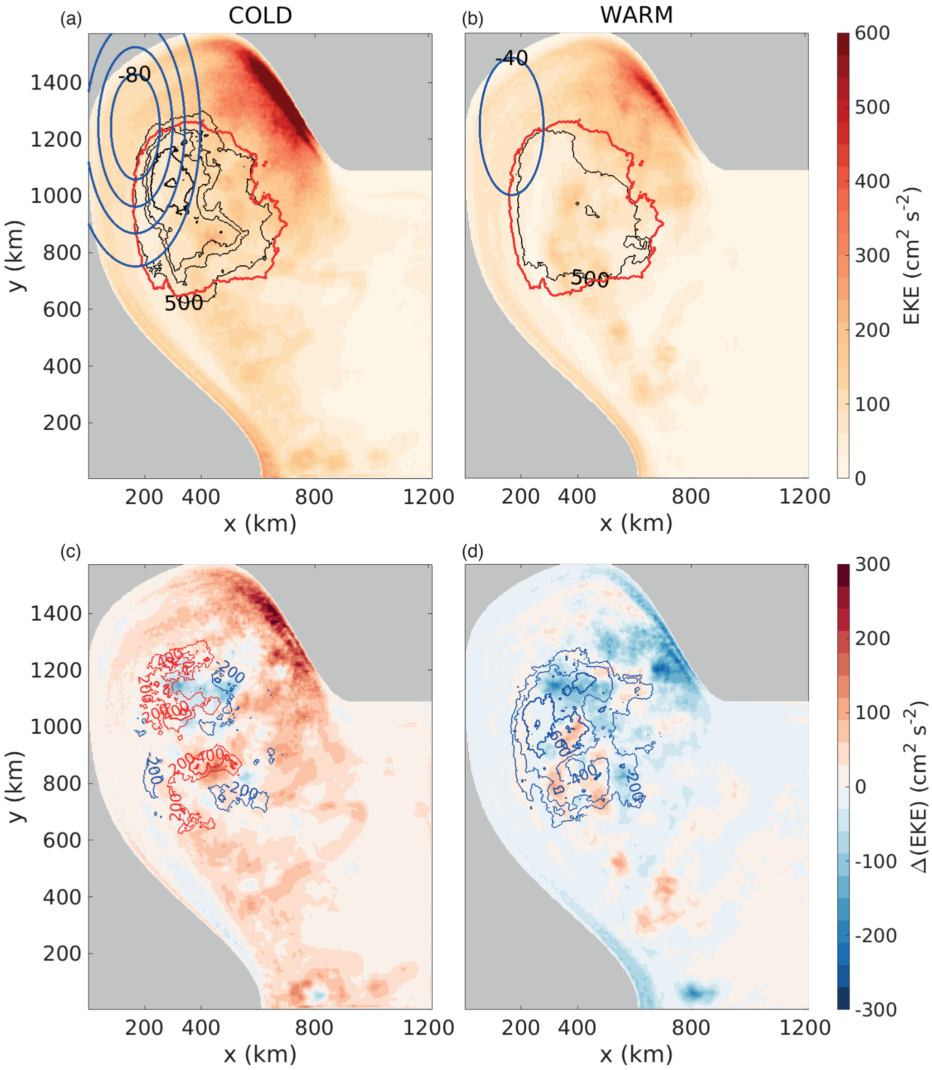

Fig. 9: (a)-(b) Wintertime (February-March) MLD and EKE, as in Fig. 4, but for the simulations (a) COLD and (b) WARM. (c)-(d) Anomalies from REF simulation of MLD (in m, contours) and EKE (in cm^2 s^{-2}, shading) for COLD and WARM, respectively. For comparison, the 500 m contour of the MLD for REF is shown in red in (a) and (b).

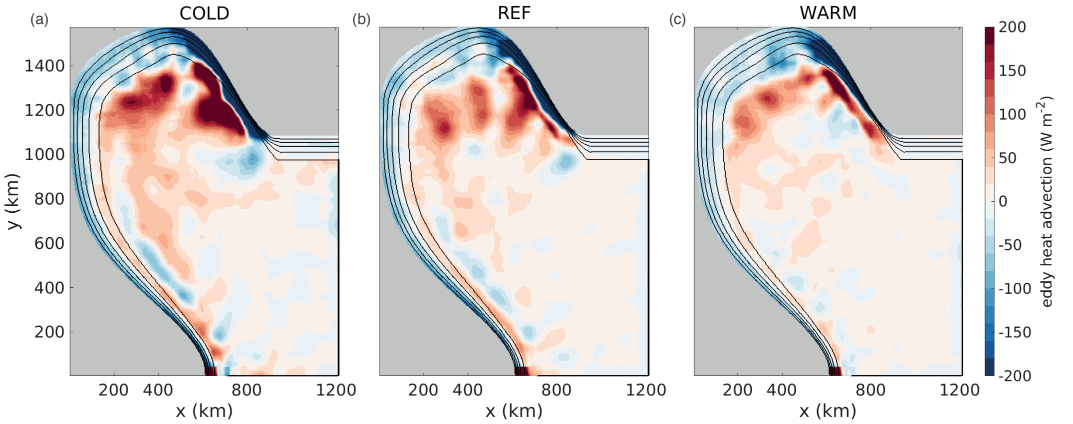

Fig. 10: Depth integrated eddy advection of heat (in W m^{-2}) for (a) WARM, (b) REF and (c) COLD. Note that panel (b) is the same as Fig. 3e and shown again here for easy comparison.

So clearly, along the entire West Greenland continental slope both the EKE and the eddy component of the advective heat flux are affected by the changes in the wintertime heat loss (Fig. 9c-d and Fig. 10). It is likely that this change in the eddy field will affect the dynamics of the downwelling and therefore its magnitude as well.

4.2. Response of the downwelling

Spall and Pickart (2001) and Straneo (2006b) state that the magnitude of the downwelling is controlled by the densification of the boundary current, suggesting that the magnitude of the downwelling will increase when the surface heat loss is stronger. Moreover, as shown in section 4.1, also the lateral eddy heat fluxes from the boundary current to the interior increase (Fig. 10), which is expected to further increase the downwelling. To assess how changes in the surface heat fluxes regulate the magnitude of the downwelling in the Labrador Sea, we also analyze the vertical velocities of the simulations COLD and WARM.

Fig. 11a shows that the time-mean vertical velocity integrated over the total domain is proportional to the applied surface heat loss. In response to an increase (decrease) of the winter heat loss by 50% compared to REF, the maximum basin-integrated downwelling increases (decreases) by 21% (-26%) or in terms of transport by +0.6 Sv (-0.8 Sv). In section 4.1, it has been shown that changes in surface heat losses influence the eddy field in the basin and this is now reflected in the magnitude of the downwelling. The downwelling in area 1 is the major contributor of the total downwelling in the basin. In COLD (WARM), the surface EKE at the west Greenland continental slope (area 1) becomes stronger (weaker) (Fig. 9c-d) and the heat loss of the boundary current increases (decreases) (Fig. 10a and Fig. 10c) resulting in an increase (decrease) of the vertical transport in this region of +6% (-18%).

Next, we investigate whether the changes in the magnitude of the downwelling (Fig. 11a) are related to changes in the properties of the boundary current in all simulations. Fig. 11b and Fig. 11c show the difference between the velocity ($\delta \mathrm{V} = \mathrm{V}_{\mathrm{outflow}} - \mathrm{V}_{\mathrm{inflow}}$) and the density ($\delta\rho = \rho_{\mathrm{outflow}} - \rho_{\mathrm{inflow}}$), respectively, at the outflow and inflow for the three simulations. In all simulations the outflow gets more barotropic. There is a slight tendency for this barotropization to increase as the applied surface heat loss is stronger. The density difference between the outflow and the inflow (Fig. 11c) shows that the upper layer of the boundary current becomes denser along the basin perimeter and that this density change increases with increasing heat loss. This can be attributed to both the surface forcing and lateral eddy heat advection of the boundary current (Fig. 10). In REF, the density of the waters at the outflow is slightly larger than at the inflow in the lower part of the boundary current (z>400 m). In COLD, this difference is larger and the opposite holds for WARM. This is in line with the view emerging from Fig. 7 that convected waters are entrained in the boundary current. The properties of the convected waters are in turn affected by the applied heat loss (i.e. denser in COLD than in WARM).

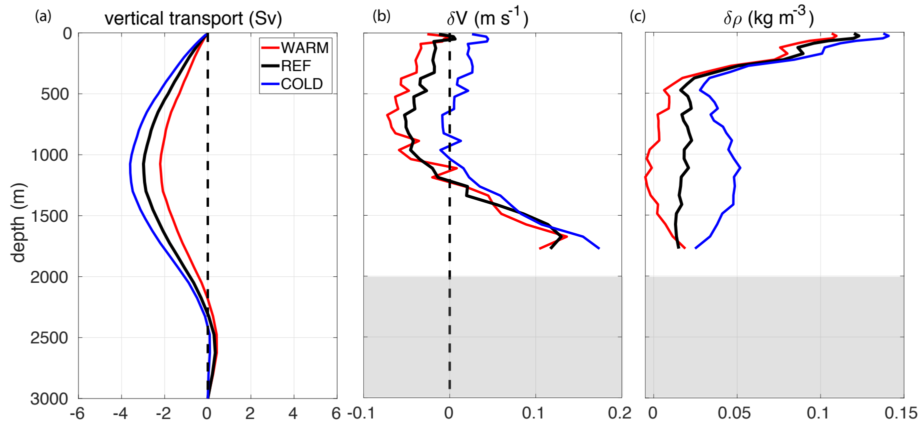

Fig. 11: (a) Vertical transport integrated horizontally over the whole domain for all the simulations. (b-c) Difference of the mean (b) velocity ($\delta\mathrm{V} = \mathrm{V}_{\mathrm{outflow}} - \mathrm{V}_{\mathrm{inflow}}$), positive denotes an increase in the boundary current velocity and (c) density ($\delta\rho = \rho_{\mathrm{outflow}} - \rho_{\mathrm{inflow}}$) of the boundary current between the eastern (close to the outflow region) and western (close to the inflow region) side of the cross section shown in the inset figure of Fig. 4b. All values are averages over the 5 years considered.

4.3. Response of the spreading of dense waters

Also in WARM and COLD we performed a tracer experiment to investigate the spreading of water masses that originate from the convection region. The tracer is initialized as described in section 3.3. Qualitatively, the behavior of the tracer in both WARM and COLD is the same as in REF, with a shallower pathway directly into the boundary current at the western side of the domain, and part of a deeper pathway towards Greenland (area 1). In all four areas, the depth at which the maximum tracer concentration occurs increases as the surface heat loss gets stronger and vice versa when the heat loss is reduced, and this is apparently affected by the convection depth. In particular, the concentration peaks at a depth of 1800 m and 1260 m for COLD and WARM in area 1, respectively (Fig. 12). Surprisingly, the amount of tracer peaks earlier (after 7 months) in both WARM and COLD (Fig. 12a and Fig. 12b, respectively) than in REF induced by more vigorous eddy field. We observe similar behavior in area 2 and area 3 (not shown). The earlier peak in the concentration of the tracer in COLD may be related to the faster export of the convected waters than in REF. The finding that the timescale of this transport from interior towards the boundary does not display a simple relation to the heat loss emphasizes once more that complex interactions exist between convection and the eddy field.

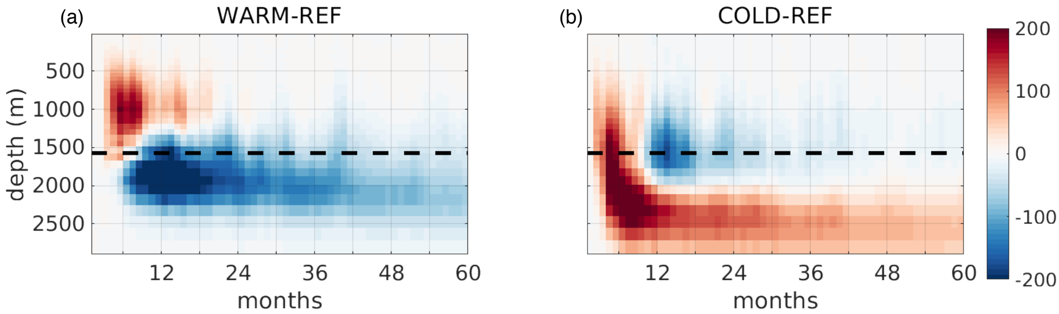

Fig. 12: Difference in the time evolution of the total amount of tracer integrated over area 1 as a function of depth for (a) WARM, (b) COLD, with respect to the REF simulation shown in Fig. 8a. The black dashed line denotes the initial maximum depth of the tracer.

5. Discussion

In the previous section, we showed that substantial downwelling is predominantly appearing in areas with strong eddy activity and the magnitude of the downwelling in these eddy-rich areas is positively correlated with the magnitude of the surface heat flux. This link between the wintertime cooling and the overturning in the North Atlantic has been pointed out in many numerical and observational studies (e.g. Biastoch et al., 2008; Curry et al., 1998), but here we demonstrate that this link is indirect (Fig. 13).

As shown in this study, both the convection and the eddy field are affected by the changes in the surface forcing. In response to a stronger (weaker) surface winter heat loss, convection is stronger and the temperature gradient between the interior and the boundary current increases (decreases). This directly impacts the eddy field; as the temperature gradient increases, the baroclinicity of the boundary current increases, and the boundary current becomes more unstable. While the generation of the eddies is known to be governed by local processes, their impacts are not restricted to their generation region since they propagate away towards the interior (Fig. 4). As a result, the associated eddy heat transport from the boundary current towards the interior strengthens (Fig. 9, Fig. 10). This increases the heat loss of the boundary current, which in turn governs the magnitude of the downwelling (Spall and Pickart, 2001; Straneo, 2006b; Katsman et al., 2018), and at the same time provides a negative feedback on the convection depth. These idealized simulations thus highlight that complex interactions between the boundary current and interior are established via the eddy activity, and in concert determine the downwelling in the basin as well as the characteristics of convection.

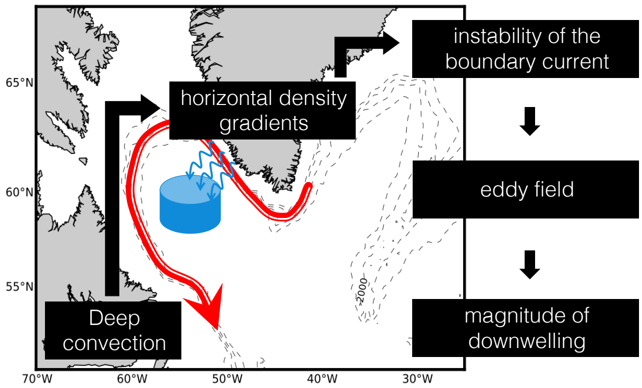

Fig. 13: Schematic showing the indirect link between convection and downwelling strength. The horizontal density gradient between the interior and the boundary current (red arrow) set by convection (blue cylinder) affects the instability of the boundary current. The eddy field and the buoyancy loss of the boundary current along the west Greenland coast govern the dynamics of the downwelling in this region.

In this study we focused on the Eulerian downwelling in depth space. This quantity is frequently used to describe the meridional overturning circulation, e.g. in the RAPID array (McCarthy et al., 2015), and in this regard it is of importance to understand the underlying physics and its sensitivity to changing surface forcing conditions. The view on the overturning based on this Eulerian downwelling differs from the view based on downwelling in density space (e.g. Mercier et al., 2015; Xu et al., 2016, 2018), which is a quantity that accounts for diapycnal processes and in particular dense water formation. While a full analysis of the watermass transformation in the basin is outside the scope of this study, we can estimate the overturning in our model using the theoretical framework outlined in Straneo (2006b).

In Fig. 4b one can clearly see a temperature difference between the eastern and western side of the displayed cross-section, which reflects the fact that the boundary current loses heat along its path. That is, the isotherms (or isopycnals) rise along the path of the boundary current between the eastern and western side of the domain. The associated reduction of the density gradient between the boundary and the interior yields a decrease of the baroclinic flow and, assuming no mass transport in cross-shore direction, a downward diapycnal transport in the boundary current (see Straneo (2006b) figure 1). An analysis of the changes in the boundary current between the inflow and the outflow region in our model simulations reveals that in all three simulations the outflow indeed gets more barotropic: the transport in the upper 1000m reduces, and the transport below that increases (Fig. 11b-c).

According to the two-layer model proposed by Straneo (2006b), the magnitude of the overturning $\mathrm{w_o}$, i.e. the transport associated with diapycnal mass fluxes from the light to the dense layer in the boundary current, can be estimated from (Eq.17 in Straneo 2006b):

$$\mathrm{w_o} = \mathrm{L}\int_0^{\mathrm{P}} \mathrm{h_2}\frac{\partial \mathrm{V_2}}{\partial \mathrm{l}}\mathrm{dl} \tag{1}$$

where L is the width of the boundary current, $\mathrm{V_2}$ the velocity of the dense lower layer, P the total perimeter of the domain and l the along-boundary coordinate. To asses $\mathrm{w_o}$ from our model simulations, we choose the $\sigma = 28.32$ kg m^{-3}, isopycnal as the boundary between the light and dense layer (Fig. 4b). We define the width of the boundary current by the location of the 18 Sv streamline of the barotropic streamfunction (vertical red line in Fig. 4b), which yields $L = 66$ km. When we average the velocity of the dense layer at inflow and outflow across the boundary current, an increase of $\Delta V_2 = +0.04$ m s^{-1} in the velocity of the denser part of the water column is found. According to Eq. 1, this yields an overturning of $\mathrm{w_o} = 2.7$ Sv, which is slightly smaller than the Eulerian downwelling calculated directly from the vertical velocity field in our model (i.e. 3.0 Sv).

The result that the changing properties of the boundary current yield an overturning does not necessarily imply that all diapycnal mixing (i.e. transformation of watermasses) takes also place within the boundary, as it has been assumed in Straneo (2006b). Our tracer analysis shows that dense waters in the interior of the Labrador Sea are directly entrained in the boundary current at shallower depths at the western side of the basin. In deeper layers, the tracer moves towards the downwelling region near Greenland (Fig. 7d-h), and is then entrained in the boundary current. Thereby, the assumption that the eddy activity only yields a lateral buoyancy transport and no mass transport, applied in the model by Straneo (2006b), may not be correct. The pathways and the timescales by which this transport of dense waters towards the boundary occurs are complex and will be addressed in more detail in a follow up study focusing on the differences and connections between the Eulerian downwelling and downwelling in density space.

6. Summary and conclusions

In this study we explore how changes in the surface heat fluxes affect the magnitude of the downwelling, the evolution of deep ocean convection in the Labrador Sea and their interplay through the eddy activity. The motivation of this study stems from the need to improve our understanding of the location where the downwelling takes place at high latitudes and its response to changes in the forcing conditions in light of a changing climate.

Under the simplifications of an idealized model for the Labrador Sea region, our analysis once more emphasizes that the presence of the IRs is crucial to balance the heat loss over the basin (Fig. 3) and to represent the restratification of the interior of the Labrador Sea (Katsman et al., 2004; Hátún et al., 2007; Gelderloos et al., 2011; de Jong et al., 2016a; Kawasaki and Hasumi, 2014; Saenko et al., 2014). In addition, this study once more underlines that with a proper representation of the mesoscale activity in the Labrador Sea the model can reproduce the winter mixed layer depths and in particular the location of deep convection (Fig. 4a) seen in observations (Pickart et al., 2002; Våge et al., 2009).

The model results show a total Eulerian downwelling in the basin of 3.0 Sv at a depth of 1000 m. Spall and Pickart (2001) estimated the magnitude of the net downward transport in the Labrador Sea, based on observations of the alongshore density variations, to be roughly of 1.0 Sv in the basin. In their recent study, Holte and Straneo (2017) used horizontal velocity sections based on Argo floats to investigate the overturning in the Labrador Sea and its variability and found a mean overturning of 0.9 ± 0.5 Sv. The total net downwelling in our idealized model is in the same order of magnitude as these observation-based estimates, albeit stronger. However, in both studies, the downwelling is deduced from the large-scale hydrography rather than observed directly and also the number of available observations is limited.

The downwelling is concentrated along the lateral boundaries and not where the heat loss is strongest or where convection is deepest. Moreover, our analysis shows that this near-boundary vertical transport is not uniform: the area where the IRs are formed contributes by far the most to the total downwelling (almost 4.0 Sv of downward transport). In addition, it has been shown that the time- and basin- mean downwelling is proportional to the applied surface heat loss, while the downwelling near the Greenland coast (area 1) displays a non-linear response to the change in heat loss.

This study emphasizes that a proper representation of the eddy field in models is one of the key elements for representing the interplay between the downwelling and convection in marginal seas at high latitudes, and their responses to changing forcing conditions. The outcome that eddies are a crucial element in the chain of events, determining changes in downwelling in the North Atlantic Ocean and hence changes in the strength of the AMOC, obviously raises the question if climate-change scenarios for AMOC changes based on coarse, non-eddy resolving climate models can properly represent the physical processes at hand. A first study that addresses this subject (Katsman et al., 2018) showed that while also in complex models the downwelling occurs near the boundary, the processes thought to govern the downwelling are not well represented in the coarse ocean model that was studied. An obvious next step is to carefully evaluate the response of the downwelling to changing forcing conditions in such coarse resolution climate models.

Acknowledgments

We kindly acknowledge the insightful comments and suggestions of three anonymous reviewers. S. Georgiou, C.G. van der Boog, N. Brüggemann and S.L. Ypma were supported by the Netherlands Organisation for Scientific Research (NWO) via VIDI grant 864.13.011 awarded to C. A. Katsman. N. Brüggemann was also partially funded by the Collaborative Research Centre TRR 181. This paper is a contribution to the project S2 (Improved parameterisations and numerics in climate models) of the Collaborative Research Centre TRR 181 "Energy Transfer in Atmosphere and Ocean" funded by the Deutsche Forschungsgemeinschaft (DFG, German Research Foundation) - Projektnummer 274762653. The model data analyzed in the current study are available from the corresponding author on request.

References

Belkin, I.M., Levitus, S., Antonov, J., Malmberg, S.A., 1998. "Great Salinity Anomalies" in the North Atlantic. Progress in Oceanography 41, 1 – 68. doi:10.1016/S0079-6611(98)00015-9.

Biastoch, A., Böning, C.W., Getzlaff, J., Molines, J.M., Madec, G., 2008. Causes of Interannual–Decadal Variability in the Meridional Overturning Circulation of the Midlatitude North Atlantic Ocean. Journal of Climate 21, 6599–6615. doi:10.1175/2008JCLI2404.1.

Böning, C.W., Behrens, E., Biastoch, A., Getzlaff, K., Bamber, J.L., 2016. Emerging impact of Greenland meltwater on deepwater formation in the North Atlantic Ocean. Nature Geoscience 9, 523–527. doi:10.1038/ngeo2740.

Bower, A.S., Lozier, M.S., Gary, S.F., Böning, C.W., 2009. Interior pathways of the North Atlantic meridional overturning circulation. Nature 459, 243–247. doi:10.1038/nature07979.

Bracco, A., Pedlosky, J., Pickart, R.S., 2008. Eddy Formation near the West Coast of Greenland. Journal of Physical Oceanography 38, 1992–2002. doi:10.1175/2008JPO3669.1.

Brandt, P., Funk, A., Czeschel, L., Eden, C., Böning, C.W., 2007. Ventilation and Transformation of Labrador Sea Water and Its Rapid Export in the Deep Labrador Current. Journal of Physical Oceanography 37, 946–961. doi:10.1175/JPO3044.1.

Brandt, P., Schott, F.A., Funk, A., Martins, C.S., 2004. Seasonal to interannual variability of the eddy field in the Labrador Sea from satellite altimetry. Journal of Geophysical Research 109, C02028. doi:10.1029/2002JC001551.

Brüggemann, N., Katsman, C.A., Dijkstra, H.A., 2017. On the vorticity dynamics of the downwelling branch of the AMOC, in: CLIVAR Exchanges Special Issue: CLIVAR Open Science Conference Award Winners, pp. 10–12.

Chanut, J., Barnier, B., Large, W., Debreu, L., Penduff, T., Molines, J.M., Mathiot, P., 2008. Mesoscale Eddies in the Labrador Sea and Their Contribution to Convection and Restratification. Journal of Physical Oceanography 38, 1617–1643. doi:10.1175/2008JPO3485.1.

Clarke, R.A., Gascard, J.C., 1983. The Formation of the Labrador Sea Water. Part I: Large-Scale Processes. Journal of Physical Oceanography 13, 1764–1778. doi:10.1175/1520-0485(1983)013<1764:TFOLSW>2.0.CO;2.

Cunningham, S.A., Kanzow, T., Rayner, D., Baringer, M.O., Johns, W.E., Marotzke, J., Longworth, H.R., Grant, E.M., Hirschi, J.J.M., Beal, L.M., Meinen, C.S., Bryden, H.L., 2007. Temporal Variability of the Atlantic Meridional Overturning Circulation at 26.5° N. Science 317, 935–938. doi:10.1126/science.1141304.

Curry, R.G., McCartney, M.S., Joyce, T.M., 1998. Oceanic transport of subpolar climate signals to mid-depth subtropical waters. Nature 391, 575–577. doi:10.1038/35356.

de Jong, M.F., Bower, A.S., Furey, H.H., 2014. Two Years of Observations of Warm-Core Anticyclones in the Labrador Sea and Their Seasonal Cycle in Heat and Salt Stratification. Journal of Physical Oceanography 44, 427–444. doi:10.1175/JPO-D-13-070.1.

de Jong, M.F., Bower, A.S., Furey, H.H., 2016a. Seasonal and Interannual Variations of Irminger Ring Formation and Boundary-Interior Heat Exchange in FLAME. Journal of Physical Oceanography 46, 1717–1734. doi:10.1175/jpo-d-15-0124.1.

de Jong, M.F., de Steur, L., 2016b. Strong winter cooling over the Irminger Sea in winter 2014–2015, exceptional deep convection, and the emergence of anomalously low SST. Geophysical Research Letters 43, 7106–7113. doi:10.1002/2016GL069596.

de Jong, M.F., Oltmanns, M., Karstensen, J., de Steur, L., 2018. Deep Convection in the Irminger Sea Observed with a Dense Mooring Array. Oceanography 31, 50–59. doi:10.5670/oceanog.2018.109.

de Jong, M.F., Van Aken, H.M., Våge, K., Pickart, R.S., 2012. Convective mixing in the central Irminger Sea: 2002-2010. Deep-Sea Research Part I: Oceanographic Research Papers 63, 36–51. doi:10.1016/j.dsr.2012.01.003.

Dickson, R., Lazier, J., Meincke, J., Rhines, P., Swift, J., 1996. Long-term coordinated changes in the convective activity of the North Atlantic. Progress in Oceanography 38, 241–295. doi:10.1016/S0079-6611(97)00002-5.

Dickson, R.R., Meincke, J., Malmberg, S.A., Lee, A.J., 1988. The "great salinity anomaly" in the Northern North Atlantic 1968–1982. Progress in Oceanography 20, 103 – 151. doi:10.1016/0079-6611(88)90049-3.

Eldevik, T., Nilsen, J.E.Ø., Iovino, D., Olsson, K.A., Sandø, A.B., Drange, H., 2009. Observed sources and variability of Nordic seas overflow. Nature Geoscience 2, 406–410. doi:10.1038/ngeo518.

Fratantoni, P.S., Pickart, R.S., 2007. The western north atlantic shelfbreak current system in summer. Journal of Physical Oceanography 37, 2509–2533. doi:10.1175/JPO3123.1.

Gascard, J.C., Clarke, R.A., 1983. The Formation of Labrador Sea Water. Part 2: Mesoscale and Smaller-Scale Processes. Journal of Physical Oceanography 13, 1779–1797. doi:10.1175/1520-0485(1983)013<1779:tfolsw>2.0.co;2.

Gelderloos, R., Katsman, C.A., Drijfhout, S.S., 2011. Assessing the Roles of Three Eddy Types in Restratifying the Labrador Sea after Deep Convection. Journal of Physical Oceanography 41, 2102–2119. doi:10.1175/JPO-D-11-054.1.

Gelderloos, R., Straneo, F., Katsman, C.A., 2012. Mechanisms behind the Temporary Shutdown of Deep Convection in the Labrador Sea: Lessons from the Great Salinity Anomaly Years 1968–71. Journal of Climate 25, 6743–6755. doi:10.1175/JCLI-D-11-00549.1.

Hátún, H., Eriksen, C.C., Rhines, P.B., 2007. Buoyant Eddies Entering the Labrador Sea Observed with Gliders and Altimetry. Journal of Physical Oceanography 37, 2838–2854. doi:10.1175/2007JPO3567.1.

Holte, J., Straneo, F., 2017. Seasonal Overturning of the Labrador Sea as Observed by Argo Floats. Journal of Physical Oceanography 47, 2531–2543. doi:10.1175/JPO-D-17-0051.1.

Johns, W.E., Baringer, M.O., Beal, L.M., Cunningham, S.A., Kanzow, T., Bryden, H.L., Hirschi, J.J.M., Marotzke, J., Meinen, C.S., Shaw, B., Curry, R., 2011. Continuous, Array-Based Estimates of Atlantic Ocean Heat Transport at 26.5 °N. Journal of Climate 24, 2429–2449. doi:10.1175/2010JCLI3997.1.

Kanzow, T., Cunningham, S.A., Rayner, D., Hirschi, J.J.M., Johns, W.E., Baringer, M.O., Bryden, H.L., Beal, L.M., Meinen, C.S., Marotzke, J., 2007. Observed Flow Compensation Associated with the MOC at 26.5 °N in the Atlantic. Science 317, 938–941. doi:10.1126/science.1141293.

Katsman, C.A., Drijfhout, S.S., Dijkstra, H.A., Spall, M.A., 2018. Sinking of Dense North Atlantic Waters in a Global Ocean Model: Location and Controls. Journal of Geophysical Research: Oceans, 123, 3563–3576. doi:10.1029/2017JC013329.

Katsman, C.A., Spall, M.A., Pickart, R.S., 2004. Boundary Current Eddies and Their Role in the Restratification of the Labrador Sea*. Journal of Physical Oceanography 34, 1967–1983. doi:10.1175/1520-0485(2004)034<1967:BCEATR>2.0.CO;2.

Kawasaki, T., Hasumi, H., 2014. Effect of freshwater from the West Greenland Current on the winter deep convection in the Labrador Sea. Ocean Modelling 75, 51–64. doi:10.1016/j.ocemod.2014.01.003.

Kulan, N., Myers, P.G., 2009. Comparing two climatologies of the Labrador Sea: Geopotential and isopycnal. Atmosphere-Ocean 47, 19–39. doi:10.3137/OC281.2009.

Lavender, K., Davis, R., Owens, W., 2000. Mid-depth recirculation observed in the interior Labrador and Irminger seas by direct velocity measurements. Nature 407, 66–9. doi:10.1038/35024048.

Lazier, J., Hendry, R., Clarke, A., Yashayaev, I., Rhines, P., 2002. Convection and restratification in the Labrador Sea, 1990-2000. Deep-Sea Research Part I: Oceanographic Research Papers 49, 1819–1835. doi:10.1016/S0967-0637(02)00064-X.

Lilly, J.M., Rhines, P.B., 2002. Coherent Eddies in the Labrador Sea Observed from a Mooring. Journal of Physical Oceanography 32, 585–598. doi:10.1175/1520-0485(2002)032<0585:CEITLS>2.0.CO;2.

Lilly, J.M., Rhines, P.B., Schott, F., Lavender, K., Lazier, J., Send, U., D'Asaro, E., 2003. Observations of the Labrador Sea eddy field. Progress in Oceanography 59, 75–176. doi:10.1016/j.pocean.2003.08.013.

Lilly, J.M., Rhines, P.B., Visbeck, M., Davis, R., Lazier, J.R.N., Schott, F., Farmer, D., 1999. Observing Deep Convection in the Labrador Sea during Winter 1994/95. Journal of Physical Oceanography 29, 2065–2098. doi:10.1175/1520-0485(1999)029<2065:ODCITL>2.0.CO;2.

Lozier, M.S., 2012. Overturning in the North Atlantic. Annual Review of Marine Science 4, 291–315. doi:10.1146/annurev-marine-120710-100740.

Luo, H., Bracco, A., Zhang, F., 2014. The seasonality of convective events in the Labrador Sea. J. Climate 27, 6456–6471. doi:10.1175/JCLI-D-14-00009.1.

Marshall, J., Adcroft, A., Hill, C., Perelman, L., Heisey, C., 1997. A finite-volume, incompressible Navier Stokes model for studies of the ocean on parallel computers. Journal of Geophysical Research 102, 5753–5766. doi:10.1029/96JC02775.

Marshall, J., Schott, F., 1999. Open-ocean convection: Observations, theory, and models. Reviews of Geophysics 37, 1–64. doi:10.1029/98RG02739.

McCarthy, G., Smeed, D., Johns, W., Frajka-Williams, E., Moat, B., Rayner, D., Baringer, M., Meinen, C., Collins, J., Bryden, H., 2015. Measuring the Atlantic Meridional Overturning Circulation at 26 °N. Progress in Oceanography 130, 91 – 111. doi:10.1016/j.pocean.2014.10.006.

Mercier, H., Lherminier, P., Sarafanov, A., Gaillard, F., Daniault, N., Desbruyères, D., Falina, A., Ferron, B., Gourcuff, C., Huck, T., Thierry, V., 2015. Variability of the meridional overturning circulation at the Greenland – Portugal OVIDE section from 1993 to 2010. Progress in Oceanography 132, 250–261. doi:10.1016/j.pocean.2013.11.001.

Moore, G.W.K., Renfrew, I.A., Pickart, R.S., 2012. Spatial distribution of air-sea heat fluxes over the sub-polar North Atlantic Ocean. Geophysical Research Letters 39. doi:10.1029/2012GL053097.

Orlanski, I., 1976. A simple boundary condition for unbounded hyperbolic flows. Journal of Computational Physics 21, 251–269. doi:10.1016/0021-9991(76)90023-1.

Pedlosky, J., Spall, M.A., 2005. Boundary Intensification of Vertical Velocity in a β -Plane Basin. Journal of Physical Oceanography 35, 2487–2500. doi:10.1175/JPO2832.1.

Pickart, R.S., Spall, M.A., 2007. Impact of Labrador Sea Convection on the North Atlantic Meridional Overturning Circulation. Journal of Physical Oceanography 37, 2207–2227. doi:10.1175/JPO3178.1.

Pickart, R.S., Torres, D.J., Clarke, R.A., 2002. Hydrography of the Labrador Sea during Active Convection. Journal of Physical Oceanography 32, 428–457. doi:10.1175/1520-0485(2002)032<0428:HOTLSD>2.0.CO;2.

Prater, M.D., 2002. Eddies in the Labrador Sea as Observed by Profiling RAFOS Floats and Remote Sensing. Journal of Physical Oceanography 32, 411–427. doi:10.1175/1520-0485(2002)032<0411:EITLSA>2.0.CO;2.

Rhein, M., Fischer, J., Smethie, W.M., Smythe-Wright, D., Weiss, R.F., Mertens, C., Min, D.H., Fleischmann, U., Putzka, A., 2002. Labrador Sea Water: Pathways, CFC Inventory, and Formation Rates. Journal of Physical Oceanography 32, 648–665. doi:10.1175/1520-0485(2002)032<0648:LSWPCI>2.0.CO;2.

Rykova, T., Straneo, F., Bower, A.S., 2015. Seasonal and interannual variability of the West Greenland Current System in the Labrador Sea in 1993-2008. Journal of Geophysical Research: Oceans 120, 1318–1332. doi:10.1002/2014JC010386.

Saenko, O.A., Dupont, F., Yang, D., Myers, P.G., Yashayaev, I., Smith, G.C., 2014. Role of Resolved and Parameterized Eddies in the Labrador Sea Balance of Heat and Buoyancy. Journal of Physical Oceanography 44, 3008–3032. doi:10.1175/JPO-D-14-0041.1.

Spall, M.A., 2004. Boundary Currents and Watermass Transformation in Marginal Seas*. Journal of Physical Oceanography 34, 1197–1213. doi:10.1175/1520-0485(2004)034<1197:BCAWTI>2.0.CO;2.

Spall, M.A., 2010. Dynamics of Downwelling in an Eddy-Resolving Convective Basin. Journal of Physical Oceanography 40, 2341–2347. doi:10.1175/2010JPO4465.1.

Spall, M.A., 2012. Influences of Precipitation on Water Mass Transformation and Deep Convection. Journal of Physical Oceanography 42, 1684–1700. doi:10.1175/JPO-D-11-0230.1.

Spall, M.A., Pickart, R.S., 2001. Where Does Dense Water Sink? A Subpolar Gyre Example*. Journal of Physical Oceanography 31, 810–826. doi:10.1175/1520-0485(2001)031<0810:WDDWSA>2.0.CO;2.

Straneo, F., 2006a. Heat and Freshwater Transport through the Central Labrador Sea*. Journal of Physical Oceanography 36, 606–628. doi:10.1175/JPO2875.1.

Straneo, F., 2006b. On the Connection between Dense Water Formation, Overturning, and Poleward Heat Transport in a Convective Basin*. Journal of Physical Oceanography 36, 1822–1840. doi:10.1175/JPO2932.1.

Straneo, F., Pickart, R.S., Lavender, K., 2003. Spreading of Labrador sea water: an advective-diffusive study based on Lagrangian data. Deep-Sea Research Part I-Oceanographic Research Papers 50, 701–719. doi:10.1016/S0967-0637(03)00057-8.

Thomsen, S., Eden, C., Czeschel, L., 2014. Stability Analysis of the Labrador Current. Journal of Physical Oceanography 44, 445–463. doi:10.1175/JPO-D-13-0121.1.

Våge, K., Pickart, R.S., Moore, G.W.K., Ribergaard, M.H., 2008. Winter Mixed Layer Development in the Central Irminger Sea: The Effect of Strong, Intermittent Wind Events. Journal of Physical Oceanography 38, 541–565. doi:10.1175/2007JPO3678.1.

Våge, K., Pickart, R.S., Sarafanov, A., Knutsen, Ø., Mercier, H., Lherminier, P., van Aken, H.M., Meincke, J., Quadfasel, D., Bacon, S., 2011. The Irminger Gyre: Circulation, convection, and interannual variability. Deep Sea Research Part I: Oceanographic Research Papers 58, 590–614. doi:10.1016/j.dsr.2011.03.001.

Våge, K., Pickart, R.S., Thierry, V., Reverdin, G., Lee, C.M., Petrie, B., Agnew, T.a., Wong, A., Ribergaard, M.H., 2009. Surprising return of deep convection to the subpolar North Atlantic Ocean in winter 2007–2008. Nature Geoscience 2, 67–72. doi:10.1038/ngeo382.

Xu, X., Rhines, P.B., Chassignet, E.P., 2016. Temperature-salinity structure of the North

Atlantic circulation and associated heat and freshwater transports. Journal of Climate 29, 7723–7742. doi:10.1175/JCLI-D-15-0798.1.

Xu, X., Rhines, P.B., Chassignet, E.P., 2018. On Mapping the Diapycnal Water Mass Transformation of the Upper North Atlantic Ocean. Journal of Physical Oceanography 48, 2233–2258. doi:10.1175/JPO-D-17-0223.1.

Yashayaev, I., Bersch, M., van Aken, H.M., 2007. Spreading of the Labrador Sea Water to the Irminger and Iceland basins. Geophysical Research Letters 34. doi:10.1029/2006GL028999.

Yashayaev, I., Loder, J.W., 2009. Enhanced production of Labrador Sea Water in 2008. Geophysical Research Letters 36. doi:10.1029/2008GL036162.

Yu, L., Jin, X., Weller, R.A., 2008. Multidecade global flux datasets from the Objectively Analyzed Air-Sea Fluxes (OAFlux) Project: Latent and sensible heat fluxes, ocean evaporation, and related surface meteorological variables. Technical Report. OAFlux Proj. Tech. Rep. OA-2008–01, Woods Hole Oceanogr. Inst., Woods Hole, Mass. URL: http://oaflux.whoi.edu/.

Zhang, W., Yan, X., 2018. Variability of the Labrador Sea Surface Eddy Kinetic Energy Observed by Altimeter From 1993 to 2012. Journal of Geophysical Research: Oceans 123, 601–612. doi:10.1002/2017JC013508.